

Semi-Supervised and Supervised Machine Learning Approaches to Predicting Fluvial Mesohabitats from Satellite Data

Elvin Cordero^{1,2} and Aubrey Harris³

Affiliation:

¹ Department of Marine Sciences, University of Puerto Rico-Mayagüez, PO Box 9000 Mayagüez, PR 00681, USA

² SeaMount Geospatial Labs, Brooklyn, NY, USA

³ US Army Corps of Engineers, Engineering Research and Development Center, Environmental Laboratory, Albuquerque, NM, USA

Corresponding Author: Aubrey Harris

- Aubrey.E.Harris@USACE.army.mil
- Phone: +1 (505) 342-3329

Research Domain: Remote Sensing, Machine Learning, Ecosystem Modeling

Funding Information: US Army Corps of Engineers' Aquatic and Nuisance Species Research Program focus on Next Generation Ecological Modeling. This research was supported in part by an appointment to the Department of Defense (DOD) Research Participation Program administered by the Oak Ridge Institute for Science and Education (ORISE) through an interagency agreement between the U.S. Department of Energy (DOE) and the DOD. ORISE is managed by Oak Ridge Associated Universities (ORAU) under DOE contract number DE-SC0014664.

Highlights:

- Semi-supervised K-means achieved 88% accuracy in mesohabitat classification.
- Demonstrates an effective, accessible change detection workflow for assessing mesohabitat change from sediment mobilization using Open-Source tools.
- Combined supervised and unsupervised methods improves classification flexibility.

Date: November 23, 2025

Abstract

High-cadence satellite data creates new opportunities for riverscape assessment provided that analyses are fast, reproducible, and robust to changing flow. This study evaluates open-source workflows for mesohabitat mapping from optical imagery, contrasting a semi-supervised clustering approach with a class-weighted supervised random forest. Two complementary targets were considered: (i) inundation (water vs. non-water) within the river corridor and (ii) direct prediction of hydraulically derived mesohabitat labels. Using PlanetScope (~ 3 m) and Landsat-9 (30 m) imagery co-registered to HEC-RAS outputs, the semi-supervised pipeline recovered inundation with high agreement (accuracy = 0.88; kappa = 0.73) and was less sensitive to sensor resolution than the supervised baseline. Time-series analysis revealed a moderate negative association between surface water and bare land area, consistent with flow-driven exposure and sediment mobilization. In a leave-one-date-out evaluation across seven flow conditions, direct mesohabitat classification from PlanetScope features achieved modest cross-date performance (mean per-pixel accuracy $\approx 0.20\text{--}0.22$; mean kappa $\approx 0.02\text{--}0.03$) but produced spatially coherent patterns (e.g., pools along thalweg, high-velocity units at constrictions), indicating learnable signal from image features alone. Results demonstrate that open, lightweight pipelines can deliver decision-ready inundation products today and provide a proof-of-concept for image-based mesohabitat mapping. Pathways to higher accuracy include restoring native spatial resolution (~ 3 m), incorporating texture and morphological context, and fusing hydraulic predictors, enabling routine, basin-scale monitoring of mesohabitat dynamics.

Keywords: Machine Learning, Google Earth Engine, Mesohabitats, Land Classification, Remote Sensing

1 Introduction

High-resolution remote sensing (RS) has transformed observation of riverscapes by enabling routine, synoptic mapping of water extent, channel morphology, and habitat structure at organism-relevant spatial grains and operational cadences (Marcus and Fonstad, 2010). Expanding public and commercial image archives, cloud platforms, and open analytical ecosystems now support ecological assessment at spatial and temporal resolutions that field data collection campaigns alone cannot sustain (Cavender-Bares et al., 2022). Field surveys remain indispensable yet are constrained by access, safety, and personnel, particularly during high flows or across difficult floodplain terrain, creating persistent gaps in coverage and frequency (Calderon and An, 2016; Griffin and Lasko, 2020; Johansen et al., 2022; Suir et al., 2023).

Within hierarchical river habitat frameworks, mesohabitats (e.g., pools, riffles/glides, runs/raceways) occupy the intermediate scale between microhabitats and reaches and exert first-order control on hydraulics, sediment processes, and aquatic assemblages (Aadland, 1993; Wegscheider et al., 2020). The spatial configuration of these mesohabitats shifts with discharge and sediment dynamics, highlighting the need for mapping approaches that are

both spatially extensive and temporally responsive (Van Rooijen and Lotsari, 2024; Zaires et al., 2021). Conventional delineation via expert field mapping and ecohydraulic modeling can achieve high fidelity but is typically limited to short river segments and sparse flow snapshots given the demands for detailed topography, boundary conditions, and calibration (Harris et al., 2024; Schwartz, 2016; Wiest et al., 2024).

Remote sensing provides an opportunity to upscale mesohabitat assessment by exploiting spectral, textural, and morphological signals. Habitat studies are increasingly using RS tools such as supervised/unsupervised land-cover classification, spectral indices (e.g., Normalized Difference Vegetation Index [NDVI], Normalized Difference Water Index [NDWI], Normalized Burn Ratio [NBR]), texture metrics, and Digital Elevation Model (DEM) derived context (e.g. slope, curvature) (Demir et al., 2018; Farwell et al., 2021; Ganesh et al., 2023; Jin et al., 2021; Li et al., 2018; McKay et al., 2022; Niedballa et al., 2022; Suttidate et al., 2023). Change-detection frameworks further enable assessment of temporal dynamics across seasons and events (Choukiker and Dohare, 2021; Lim et al., 2018; Romero et al., 2016; Zimmermann et al., 2007).

A large body of work has leveraged Geographic Object-Based Image Analysis (OBIA) to map riverscape units by coupling image segmentation, spectral features, and contextual/topographic constraints. Hierarchical, multiscale OBIA that fuses very high resolution (VHR) imagery with LiDAR has produced accurate maps of channels, bars, riparian vegetation, and, in some cases, in-channel mesohabitats (Demarchi et al., 2016a, 2016b; Kutz et al., 2022; Shabat and Tapamo, 2017). Yet performance can be sensitive to segmentation parameters and scene complexity, with transferability across dates, sites, and flow states often requiring retuning, especially where specular reflection, turbidity, shadows, and narrow channels degrade separability (Wang et al., 2019; Wurm et al., 2019; Zhang et al., 2023).

Machine learning (ML) and deep learning have expanded capabilities by learning features directly from data. Convolutional neural networks (CNNs), classification and representation learning models; and other classical ML models provide robust baselines and ensembles for tabular/image features (Aggarwal, 2018; Howard and Gugger, 2020; Kuhn, 2008; Lantz, 2023; Ma et al., 2019; Thompson and Brodrick, 2021). In fluvial contexts, deep learning networks at sub-meter resolution can exploit texture and spatial context to classify water and hydraulically relevant surface states—even with limited spectral bands—while hybrid workflows integrating image-derived flow texture with terrain cues have distinguished glides, riffles, and pools across discharge conditions (Brostow et al., 2009; Moortgat et al., 2022; Romero et al., 2016; Shashikant, 2019; Verma et al., 2021). These developments suggest that mesohabitat categories may be predictable directly from imagery, provided appropriate annotations and cross-date validation.

Sensor choice is important; coarser sensors (10–30 m) incur mixed pixels in narrow channel widths, whereas most VHR constellations trade spatial grain against temporal cadence. PlanetScope (~3 m, near-daily) offers a pragmatic balance for riverscape monitoring and has seen wide uptake across aquatic and terrestrial applications (Planet Labs PBC, 2024). National aerial programs (e.g., National Agriculture Imagery Program [NAIP]; U.S. Geological Survey [USGS] 1-m orthoimagery) provide sub-meter data but at lower or irregular temporal frequency, complicating multi-date analyses tied to flow (USDA, n.d.; USGS, 2023a,

2023b, 2011). Persistent challenges include assembling labeled datasets at scale, coping with class imbalance among mesohabitats, and ensuring robustness to domain shifts in color, turbidity, substrate, and illumination (Mandlik and Mundhe, 2018; Maskey et al., 2018; Vahidi et al., 2023).

Despite substantial advances, an operational gap remains: can mesohabitat types be predicted directly from satellite features across streamflow regimes, without reliance on site-specific LiDAR or dense field annotation, and with validation that is explicitly out-of-time and hydrologically aware? Object-based pipelines often require site/timestep retuning and can degrade under heterogeneous riverscape conditions (i.e. specular reflection, shadows, turbidity), limiting transferability (Demarchi et al., 2016a, 2016b; Kutz et al., 2022; Zhang et al., 2023). Deep learning and modern ML offer stronger representation capacity but remain sensitive to label scarcity, class imbalance, and domain shift across color/turbidity/illumination (Aggarwal, 2018; Fix and Hodges, 1989; Ma et al., 2019; Maskey et al., 2018; Vahidi et al., 2023; Wang et al., 2019; Wurm et al., 2019). Moreover, ecohydraulic mapping at scale is constrained by the cost and data demands of LiDAR-driven or fully calibrated hydraulic models (Lindenschmidt and Carr, 2018; Schwartz, 2016). Because mesohabitat composition shifts with discharge, models must respect flow dependence and test temporal generalization (Aadland, 1993; Harris et al., 2024). These considerations motivate a label-efficient, imagery-first strategy that exploits high-cadence VHR sources (e.g., Planet) for multi-date coverage while limiting mixed-pixel issues typical of coarser sensors in narrow channel widths (Planet Labs PBC, 2024; USGS, 2023c)

This study advances riverscape mapping by testing whether mesohabitat classes can be inferred directly from high-resolution satellite features across varying discharges, rather than relying on inundation proxies. Focusing on the Big Blue–Kansas Rivers confluence (Manhattan, KS), the work (i) establishes reach-scale baseline landcover land-use (LULC) and mesoscale change products for context and continuity, and (ii) evaluates image-based prediction of eight hydraulically defined mesohabitats using PlanetScope imagery (Planet Labs PBC, 2024) due to its consistent, near-same-day coverage of all modelled dates. The central objective is to quantify how well satellite-only predictors recover mesohabitat labels under temporally out-of-sample conditions and to benchmark those results against the simpler inundation classification, delivering categorical prediction maps and cross-date performance summaries suitable for monitoring and management. All analyses are implemented with open, reusable tooling to maximize transparency and transferability.

2 Methodology

2.1 Software & Data Requirements

The geospatial processing procedure was completed for the data prior to the statistical analysis utilizing the R statistical language (R Core Team, 2023). A suite of R spatial tools including the *terra*, in concert with the *tidyterra* and *rgee*, were used for the data acquisition steps (Aybar et al., 2020; Hernangómez, 2023; Hijmans, 2024). The *rgee* package is a nested wrapper that connects R to the Google Earth Engine (GEE) Web REST API via the GEE Python API (Aybar et al., 2024; Eltayeb Elmahal and Mahmoud Ibrahim Musa, 2023). The USGS discharge data from the nearest sites on the Kansas River (#6879100 Fort Riley and #6887500 Wamego) and the Big Blue River (#6887000 Manhattan) were downloaded by using the R package *dataRetriever* (De Cicco et al., 2023) (Fig. 1b-c). The R package *tidymodels* was used to employ the ML methods (Kuhn and Wickham, 2020). Polygon drafting and editing was done in the QGIS geographic information system software (QGIS Development Team, 2024).

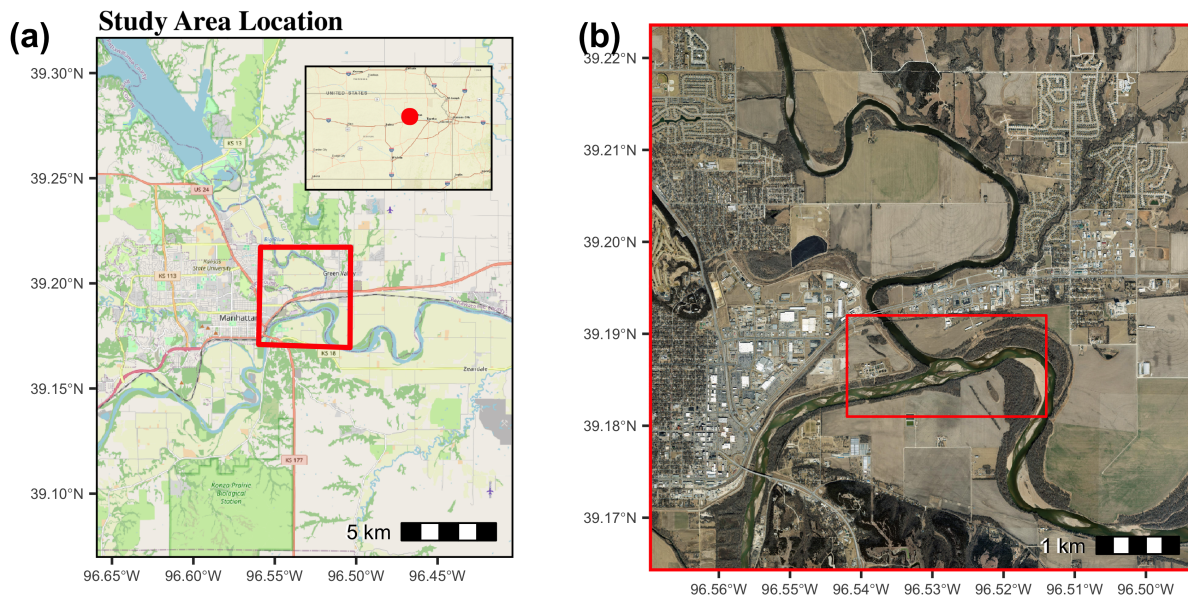


Fig. 1. The red square in left panel (a) represents the study area (b) which is adjacent to the city of Manhattan, Kansas, located roughly 200 kilometers west of Kansas City Metropolitan Area, United States (see inset map of (a)). The red square in the right panel (b) represents the location of the zoomed in portion of the subsequent figures.

2.2 Geospatial Preprocessing

The area of interest (AOI) is located at the confluence of the Big Blue and Kansas Rivers in the greater Manhattan, Kansas Area (Fig. 1). The analysis domain was restricted to the river corridor by applying a 30-m (98.4252-ft) buffer to the USGS Watershed Boundary Dataset's (WBD) waterbody layer (USGS, 2023d). The river corridor was later manually adjusted to include pointbars and other portions of the river corridor that were beyond the

buffer area from the WBD. Because of the low resolution of the raster data, tributaries were excluded from the analysis.

Landsat-9 (30-m) satellite images collected between November 21st, 2021 and November 14th, 2023 were retrieved via GEE (USGS, 2023c). Images with more than 20% cloud cover were excluded from the collection. In total, there was a refined collection of 22 images covering all seasons (Fig. 2). The Landsat-9 imagery bands used for the analysis contain seven bands including the coastal aerosol, blue, green, red, near infrared (NIR), and two shortwave infrared (SWIR) bands (Fig. 2). Similarly, higher resolution (3-m) satellite images from the same time period from the PS2, PS2.SD, and PSB.SD satellites from the PlanetScope constellation were collected for the same time period (Planet Labs PBC, 2024). Since the PlanetScope inventory contained several snapshots of the AOI on a daily basis, sometimes multiple times a day, only images with 0% cloud cover were included. The PlanetScope imagery was limited to the blue, green, red, and NIR bands. The data for the 22 images were combined into two raster stacks, one for Landsat and another for PlanetScope, with a combined total of 154 and 88 bands respectively.

Landsat Satellite Data

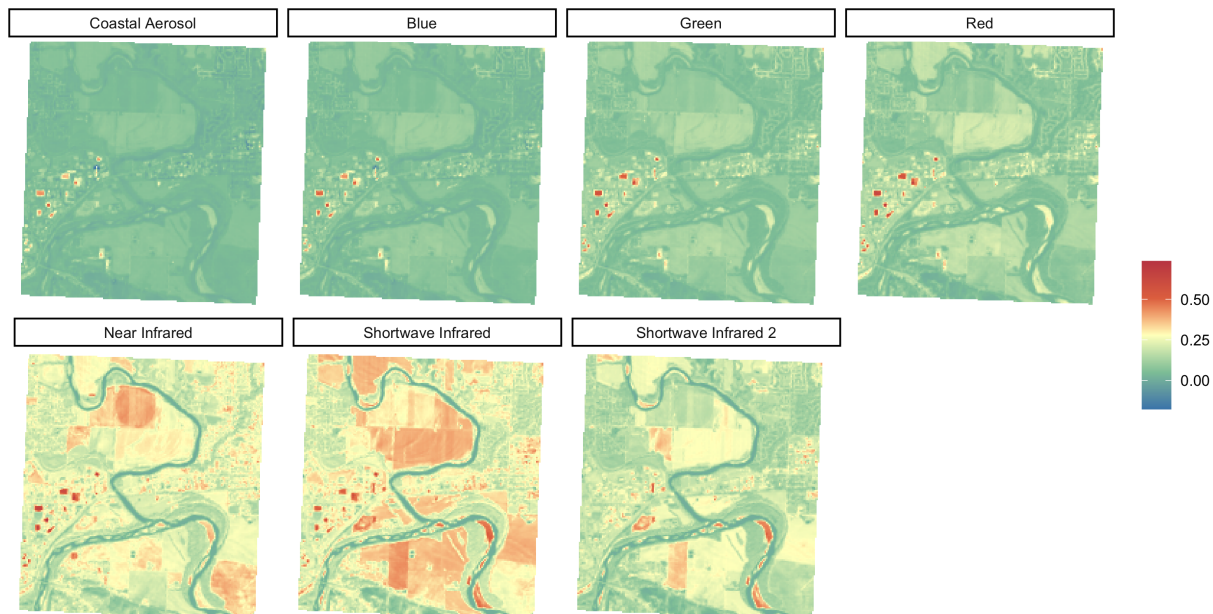


Fig. 2. Landsat-9 satellite image captured on 11-21-2021 and extracted from Google Earth Engine with each band displayed as a different sensor. The legend values indicate normalized surface reflectance (unitless).

2.2.1 Aquatic Mesohabitat Types and Surface-Water Baseline Distribution

Aquatic mesohabitat types were defined from a 2D HEC-RAS simulation on a 3-m grid using depth–velocity thresholds consistent with mesoscale typologies (Aadland, 1993; Wiest et al., 2024). Classes comprised (1) shallow pool, (2) medium pool, (3) deep pool, (4) fast riffle, and (5) raceway, (6) faster than a raceway, and (7) faster than a deep pool. Seven hydrologic snapshots spanning the site's discharge regime were selected from USGS

mean-daily flow records via the *dataRetrieval* package (De Cicco et al., 2023): 2021-12-22 and 2022-02-12, 2022-04-17, 2022-05-31, 2022-06-20, 2022-07-18, and 2022-09-28 (Fig. 3).

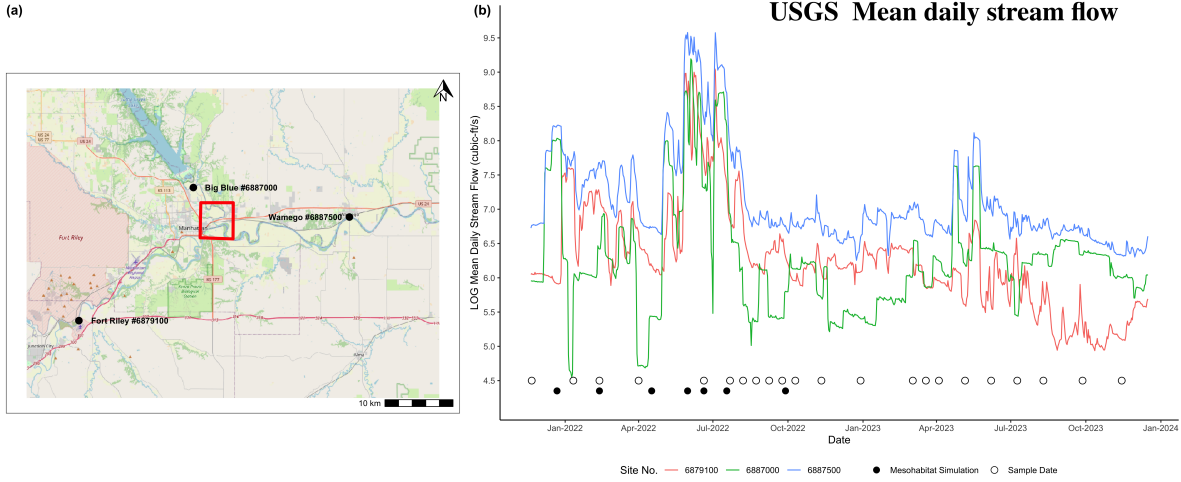


Fig. 3. (a) Stream gauge data from three USGS sites (Fort Riley No.6879100, Wamego No.6887500, Manhattan No.6887000) near the study area, outlined in red, were used to identify seven dates with diverse flow conditions (filled circles in [b]). (b) Mean daily stream flow (cubic-ft/s), lines colored by site No.

2.3 Semi-Supervised Classification

A semi-supervised classification approach was used to categorize the imagery into five classes: urban, bare land, non-forest vegetation, forested land, and surface water. This ensemble approach involved clustering the data into unsupervised classes using a K-means approach and then classifying unseen data based off the new classes using a supervised K-Nearest Neighbors (KNN) approach. The Hartigan-Wong K-means algorithm was chosen to classify the image, which seeks the local optima by shifting points from one cluster to another to assign the point to the cluster with the smallest within-cluster sum of squares (Hartigan and Wong, 1979).

Transitioning from unsupervised to supervised learning, KNN is introduced as the classification algorithm. KNN is inherently simple yet effective: for a given new instance, it identifies K nearest data points based on a distance metric (e.g. Euclidean distance) and assigns the new instance to the most common class among its K nearest neighbors. The integration of K-means clustering and KNN allowed us to utilize the structure discovered in unlabeled data to classify new data points. The assumption here is that the clusters formed during the K-means phase are meaningful and represent different categories that can be used for classification.

2.4 Supervised Classification

A supervised approach was used to classify pixels into five general classes - bare land , non-forest vegetation (i.e. shrubby, scattered brush, or grasslands, etc.), forest, urban, and

water based off the Anderson land cover classification (Anderson et al., 1976). Land cover classes were manually delineated within the AOI, each assigned one of the classes using QGIS (QGIS Development Team, 2024). Only pixels that remained unchanged within the study period were delineated to reduce the variation between dates.

Training for a random forest classification model was performed on 80% of the class delineated pixels. The number of trees was set to 1000. Model tuning parameters were ascertained via testing different configurations on a five-fold cross-validation resampling of the training data at 50m resolution. The highest accuracy and Receiver Operating Characteristic Area Under the Curve (ROC AUC) were used as indicators for picking the best modeling parameters. Two parameters were tested: (1) minimum n, identified as the minimum number of data points in a node that are required for the node to be split further, and (2) the number of predictors that will be randomly sampled at each split when creating the tree models.

The trained random forest model was used to predict the pixels across the AOI for the raster stacks, creating a classified raster representing the average conditions within the two-year period of image collection. Additional, individual random forest models using the same model parameters were produced and applied to the image pixels to create a classified raster corresponding to each date.

2.5 Time Series Analysis

The ML-classified rasters were masked to the river corridor to limit the noise in the results. The average cell size was converted to acres ($1\text{m}^2 = 0.00024711$ acres) and was multiplied by the total number of observations to estimate the total area per class. Two differencing techniques were implemented to detect temporal change: (1) difference in total area between an image date and the following image date was calculated by subtracting the area by the lag-one area and (2) the difference between the image date and the baseline condition raster using the following set of equations:

$$area_{\delta 1} = \sum_{i=1}^n area_{t_n} - \sum_{i=1}^n area_{t_{n+1}}, \quad (1)$$

$$area_{\delta 2} = \sum_{i=1}^n area_{t_0} - \sum_{i=1}^n area_{t_n}, \quad (2)$$

Where $area$ is the total area, $area_{\delta 1}$ is the temporal change in total area between consecutive dates, $area_{\delta 2}$ is the change relative to the baseline condition, t_0 is the baseline condition, t_n represents a sampling date, and t_{n+1} is the following sampling date.

2.6 Model Evaluation

2.6.1 Comparison Analysis

To evaluate whether mesohabitat types can be predicted directly from satellite data, rather than inferring inundation, HEC-RAS-derived mesohabitat maps (Aadland, 1993; Wiest et al., 2024) were used as categorical ground truth, and image-based models were trained to predict eight classes: Shallow Pool, Med Pool, Deep Pool, Fast Riffle, Raceway, Faster than a Raceway, and Faster than a Deep Pool. PlanetScope imagery for each date was co-registered to the mesohabitat grid, and three indices were derived from the four bands: Normalized Difference Vegetation Index (NDVI), Normalized Difference Water Index (NDWI), and a SWIR-free normalized burn-ratio (NBR) proxy suitable for sensors without SWIR (e.g., PlanetScope).

$$NDVI = \frac{NIR - Red}{NIR + Red} \quad (3)$$

NDVI highlights vegetation; values near +1 indicate dense green cover.

$$NDWI = \frac{Green - NIR}{Green + NIR} \quad (4)$$

NDWI enhances open-water detection via Green–NIR contrast.

$$NBR_b = \frac{NIR - Blue}{NIR + Blue} \quad (5)$$

NBR_b is a SWIR-free analogue of the NBR, responsive to moisture/substrate changes.

These indices were used as spectral predictors to train the mesohabitat classification models. Predictors were restricted to PlanetScope because it was the only sensor providing consistent, near-same-day coverage for all seven hydraulic-model dates at this site, yielding a complete, largely cloud-free stack aligned to the mesohabitat observations. Landsat-9 imagery exhibited gaps and cloud contamination on several target dates and introduced mixed-pixel issues for narrow channel features; inclusion would have necessitated dropping dates or resampling labels inconsistently. To reduce computation and harmonize supports, PlantScope rasters were aggregated by a factor of five (spectral bands averaged; mesohabitat labels aggregated by modal vote), yielding a working cell size of ~15 m.

A leave-one-date-out (LOO) design was adopted to respect the flow-dependence of mesohabitats: for each held-out date (Dec 22 2021; Feb 12, Apr 17, May 31, Jun 20, Jul 18, and Sep 28 2022), models were trained on the remaining six dates and evaluated on the hold-out. Two modeling approaches were compared:

1. **Semi-supervised clustering:** Features were standardized; K-means was fit on training pixels ($k = 12$; $nstart = 10$). Each cluster was assigned a mesohabitat label by majority vote over training labels. The held-out date was predicted by nearest-center assignment

in the standardized space.

2. **Supervised random forest:** A class-weighted random forest (800 trees, `mtry` \leq 6, `min_n` = 5) was implemented via the R `tidymodels/ranger` packages. Class weights were set inversely proportional to class frequency in the training fold to mitigate imbalance. Predictors comprised the four bands plus the three indices.

All modeling and evaluation were restricted to the mesohabitat mask (i.e. the river corridor). Performance was summarized per fold using overall accuracy and Cohen's kappa; prediction maps for each held-out date were exported as categorical rasters.

3 Results

3.1 Median Mesohabitat Distribution

For each snapshot, the hydraulic model produced a categorical mesohabitat map. A surface-water baseline mask was then derived as the per-pixel median mesohabitat state across the seven dates (Fig. 4); pixels outside this median mesohabitat distribution were treated as non-water. Cloud-free PlanetScope scenes acquired on or near the same dates of mean-daily flow records (Fig. 3) were co-registered to the hydraulic grid, and model performance for the water vs. non-water task was evaluated using confusion matrices against this baseline.

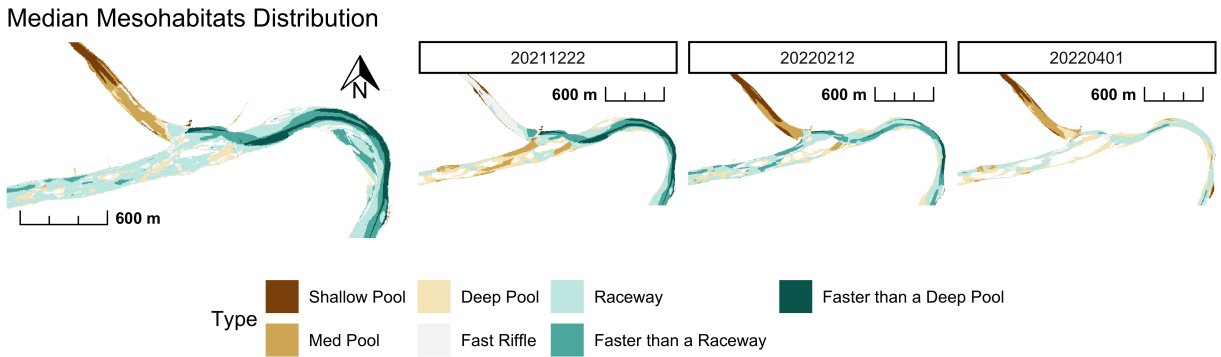


Fig. 4. Predicted distribution of mesohabitats within the study area between December 2021 and September 2022 (see study area figure for reference location). Left panel displays the median distribution of mesohabitat types, which in aggregation represents the distribution of surface water. Right panel displays the mesohabitat types predicted for three of the seven mesohabitat sampling dates: December 22nd, 2021 and February 25th, 2022, and April 4th, 2023.

3.2 Optimized Semi-Supervised Clustering

With consideration of the elbow method for finding the optimal k for the K-means clustering, i.e., the number of clusters, it was determined that k between two and 15 is ideal, which is still subjective (Fig. 5). A silhouette analysis provided a measure of the similarity between an object and the objects in its own cluster versus the other clusters. Six clusters produced the highest average silhouette width and was therefore chosen as the optimal value of k (Fig. 5). The algorithm was allowed to converge at up to 500 iterations. The K-means model was applied to the entire image collection to establish baseline condition during the study period. Each cluster produced from the K-means model was treated as a distinct class (vegetation, forest, water, and mixed/bare land [either bare land or urban]) which were used to train the KNN model (Fig. 6).

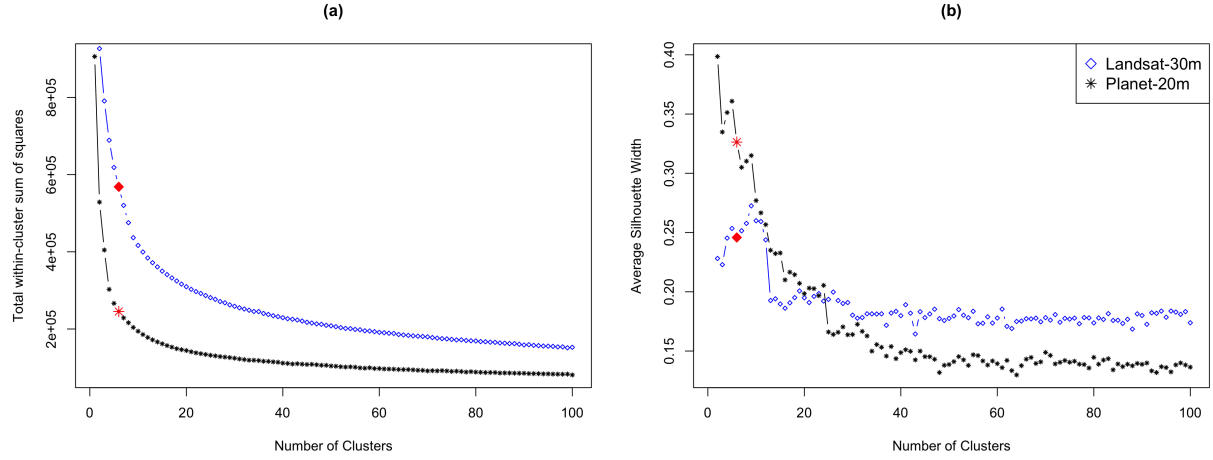


Fig. 5. K-means cluster quality was reviewed using the (a) elbow and (b) silhouette methods for Landsat-9 versus PlanetScope satellite imagery. Points highlighted in red identify the location of the optimal k value chosen for the number of clusters.

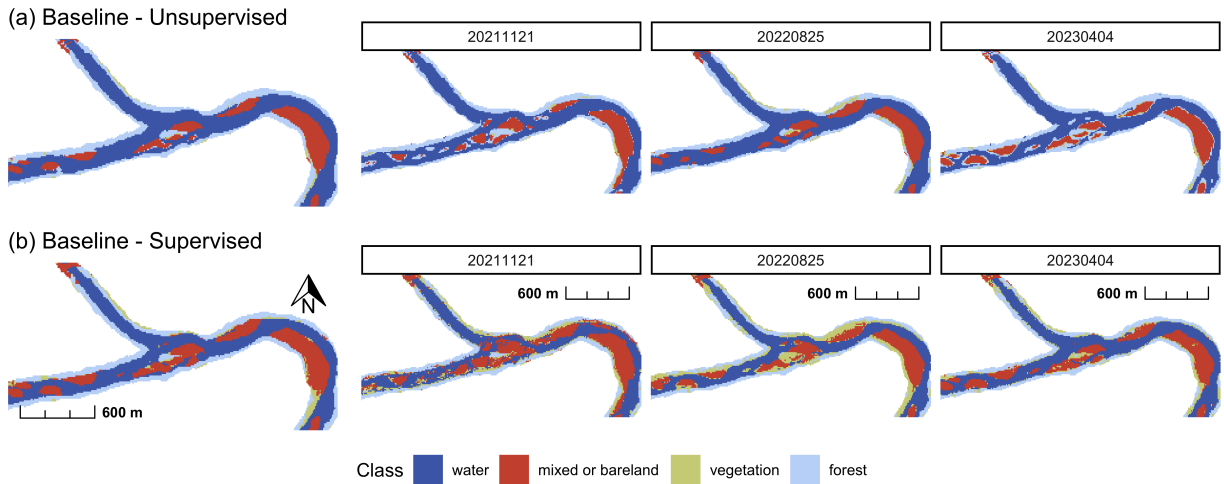


Fig. 6. Predicted distribution of landcover types (a) from the unsupervised and (b) supervised models zoomed into the confluence of the Big Blue and Kansas Rivers (see study area figure for reference location). Left panel displays the baseline/static distribution of landcover types. Right panel displays the landcover types predicted for three of the 22 sampling dates: November 21st, 2021, August 25th, 2022, and April 4th, 2023.

3.3 Optimized Supervised Learning Model

Testing revealed that the highest parameter-specific AUCs (> 0.9975) for the random forest models were achieved when minimum n and number of predictors were in between one to 20 and two to 25, respectively (Fig. 7(a)). The highest AUC was achieved when minimum n is set to seven and the number of predictors was set to six, therefore, these values were implemented in the random forest model (Fig. 7(b)).

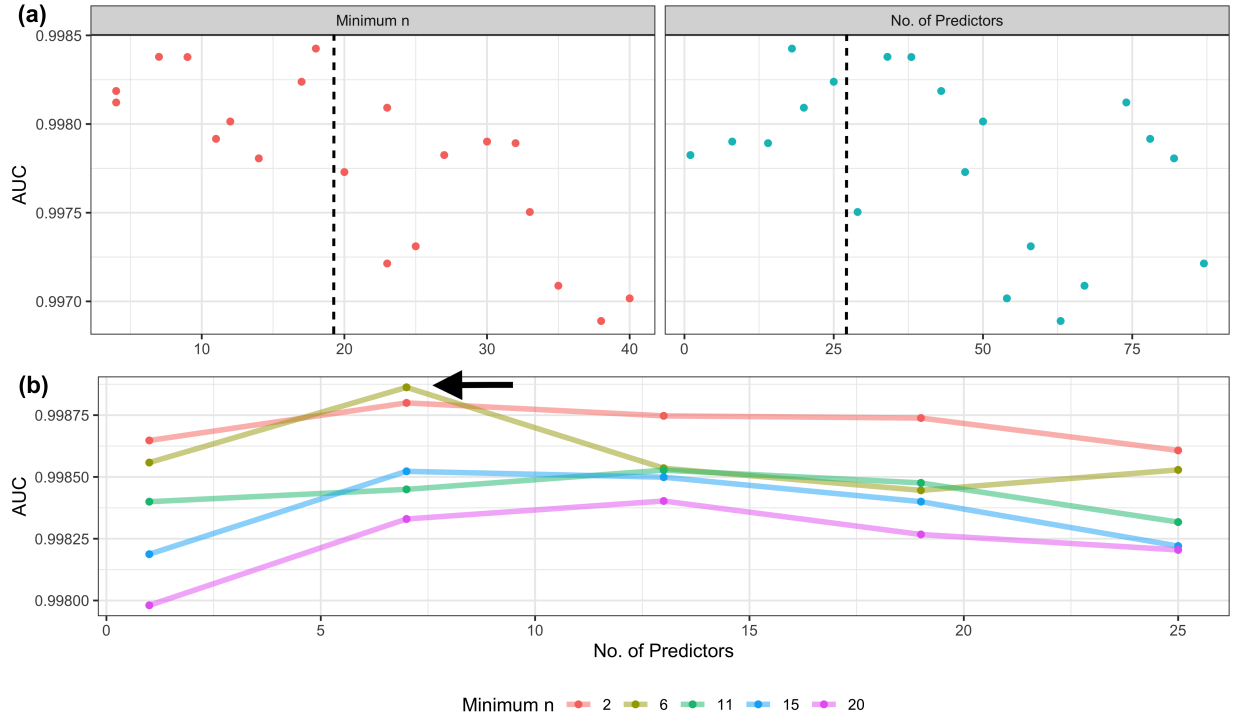


Fig. 7. The random forest parameters including minimum number of data points in a node and the number of predictors randomly sampled at each split were tuned by testing several configurations of random forest models with 1000 trees. The "best" area under the curve (AUC) was used as the configuration for the random forest model. (a) The optimal parameter-specific AUCs (before the dashed line) were used to test variations of the optimal tuning parameters (b). The arrow represents the highest AUC achieved, representing the best tuning parameters for the data.

3.4 Model Summary and Performance

3.4.1 Surface Water Validation

In terms of detecting change in LULC type, there were five comparable classes: urban, bare land, non-forest vegetation, forested land, and surface water. There were several differences between the higher resolution PlanetScope dataset and the lower resolution Landsat dataset. Notably, the PlanetScope data produced less variable results than Landsat data, except for forested land and surface water for the semi-supervised and supervised ML models, respectively (Fig. 8[a-b]). Across both datasets, the average bare land area predicted by the semi-supervised model was consistently higher than that predicted by the supervised model. For instance, in the Landsat dataset, the semi-supervised model predicted 147.83 acres compared to 55.53 acres by supervised model. Similarly, in the PlanetScope dataset, the semi-supervised model predicted 102.25 acres, while the supervised model estimated 91.59 acres (Table 1).

Overall within-class variation was generally low for the bare land and water classes (Fig. 8[a-b]). Specifically, the change in area over time and difference in area from baseline conditions was less variable for bare land in the supervised model and water in the semi-supervised model (Fig. 8[a-b]). For surface water, the models produced comparable average

predictions, with semi-supervised model estimating 372.81 acres and 372.51 acres for Landsat and Planet, respectively, and supervised model estimating more than 70 acres less acreage (293.45 acres and 302.86 acres) (Table 1).

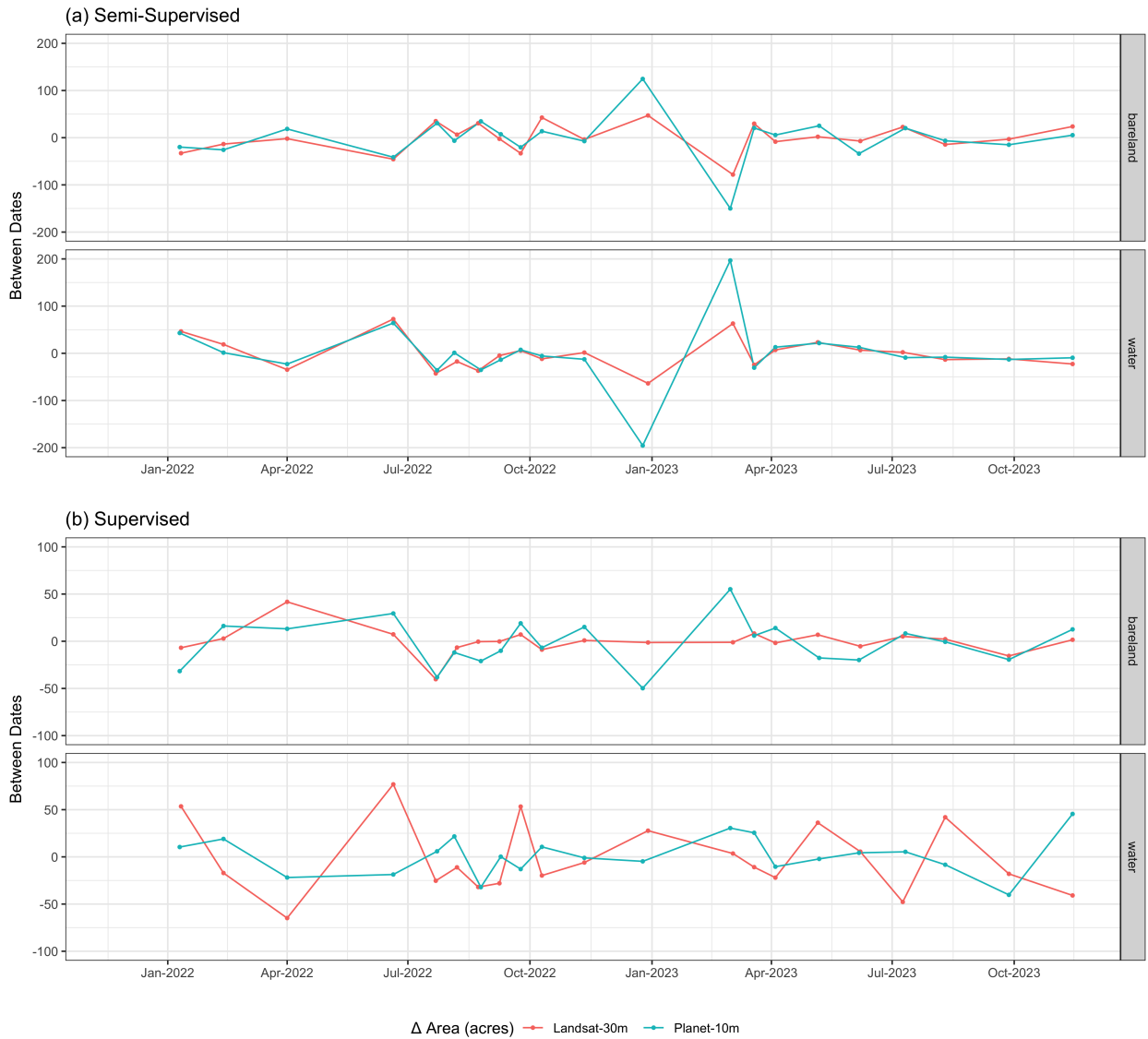


Fig. 8. Image difference, $\text{area}_{\delta 1}$, measure calculated using the difference in area from one sampling date to the following date.

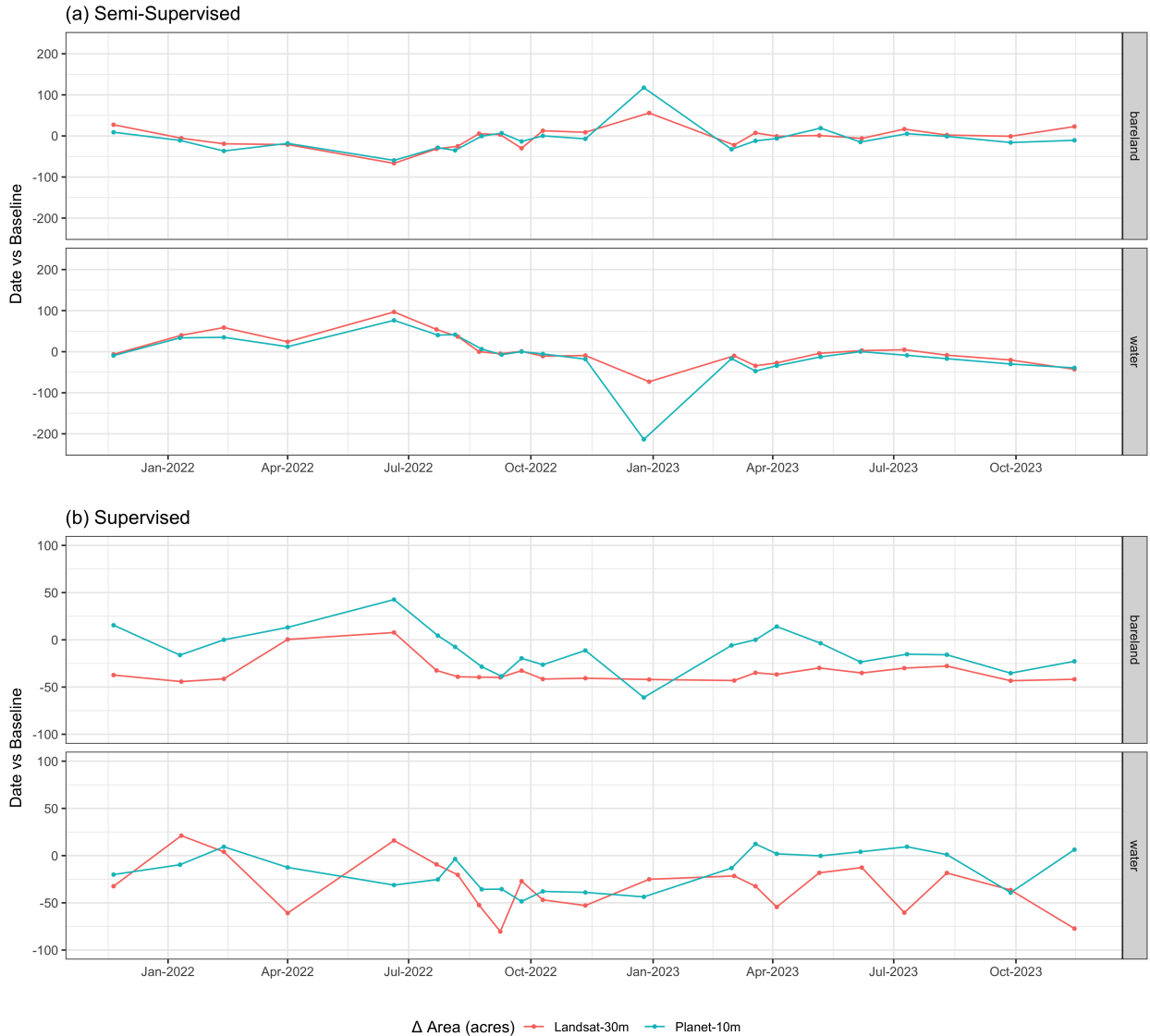


Fig. 9. Image difference, $\text{area}_{\delta 2}$, measure calculated using the difference in area between the baseline conditions and the sampling date.

In comparison, the semi-supervised model predicted ~ 2.71 times the amount of bare land than the supervised model in the Landsat dataset, but relatively similar predictions in the PlanetScope dataset (Table 1). Regardless of the source data, the semi-supervised model predicted more than 1,300-1,500 and 1,500-1,600 acres of surface water and forested land, respectively, while the supervised model predicted 2,000-2,500 acres non-forest vegetation (Table 1). There was roughly ~ 2.5 times acreage of urban land cover predicted from the Landsat derived supervised model than the similar model derived from Planet. Both models generated similarly conservative outputs for surface water (Table 1).

Due to the non-normality and limited data points, a Kendall's tau correlation coefficient was computed to test the relationship between the bare land and surface water landcover types. The results revealed that changes in surface water and bare land were moderate

negatively correlated (-0.49 and -0.39 in the Landsat and PlanetScope datasets, respectively) for the semi-supervised model (Figures 8(a)-9(a)). Positive changes in surface water area led to negative changes in bare land , and vice versa. Theoretically, this correlation is expected as the river corridor alternates between submersion at higher flows and islands exposure at low flows. Similar patterns were not discernable for the supervised model, where Kendall's tau produced a weakly correlated relationship (0.04 and 0.06 in the Landsat and PlanetScope datasets, respectively) (Figures 8(b)-9(a)).

Table 1. Summary of average and total area (acres) of bare land and surface water predicted by the ML models.

Area	Class	Landsat		Planet	
		Semi-Supervised	Supervised	Semi-Supervised	Supervised
Average	water	372.81	293.45	372.51	302.86
	water	8201.84	6455.95	8195.18	6663.02
Total	water	372.81	293.45	372.51	302.86
	water	8201.84	6455.95	8195.18	6663.02

A confusion matrix comparing the baseline surface-water condition predicted by the unsupervised and supervised learning models (created during the comparative analysis) against the HEC-RAS-derived median mesohabitat distribution showed that the semi-supervised model correctly classified approximately 65 more acres of water relative to the supervised model (Table 2). The supervised model performed slightly better at classifying non-water conditions (Table 2). Overall, the semi-supervised approach outperformed the supervised model on all reported metrics, including an accuracy of 0.88 and a kappa value of 0.73 (Table 3).

Table 2. Confusion table of the predicted model versus observations of water for classified mesohabitats.

Model	Prediction	Observed	
		not water	water
Semi-Supervised	water	12	292
	water	1	225
Supervised	not water	124	45
	not water	135	113

Table 3. Performance metrics of the predicted model versus observations of surface water derived from classified mesohabitats.

Model	Acc	Kappa	Sens	Spec	Pos Pred Val	Neg Pred Val	Matthews J- Corr Coef	J- index	Bal Acc	Det Prev	Prec	Recall	F Meas
Semi-Supervised	0.88	0.73	0.91	0.87	0.73	0.96	0.73	0.78	0.89	0.36	0.73	0.91	0.81
Supervised	0.76	0.53	0.99	0.67	0.55	1.00	0.60	0.66	0.83	0.52	0.55	0.99	0.70

3.4.2 Mesohabitat Label Prediction

The LOO evaluation across seven dates yielded mean (\pm SD) per-pixel accuracy of 0.149 ± 0.06 for the semi-supervised model and 0.208 ± 0.083 for the supervised model; mean

Cohen's kappa was -0.001 ± 0.026 and 0.026 ± 0.024 , respectively (Tables 4, 5). Accuracies varied by date (semi-supervised range: 0.052–0.218; supervised range: 0.084–0.352), reflecting differences in class composition among folds (Table 4). Categorical prediction rasters were generated for each held-out date (Fig. 10; Tables 4, 5).

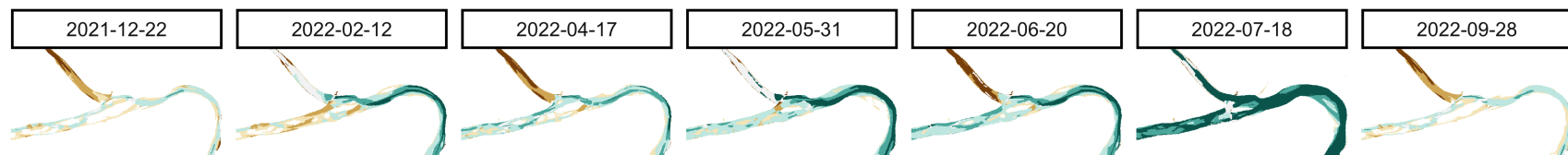
Table 4. LOO per-fold mesohabitat classification performance.

Date	Model	Accuracy	Kappa
2021-12-22	Semi-Supervised	0.209	0.006
	Supervised	0.198	0.049
2022-02-12	Semi-Supervised	0.181	-0.021
	Supervised	0.265	0.058
2022-04-17	Semi-Supervised	0.116	-0.005
	Supervised	0.352	0.045
2022-05-31	Semi-Supervised	0.052	-0.007
	Supervised	0.084	-0.006
2022-06-20	Semi-Supervised	0.158	0.024
	Supervised	0.209	0.016
2022-07-18	Semi-Supervised	0.112	0.036
	Supervised	0.175	0.011
2022-09-28	Semi-Supervised	0.218	-0.040
	Supervised	0.175	0.012

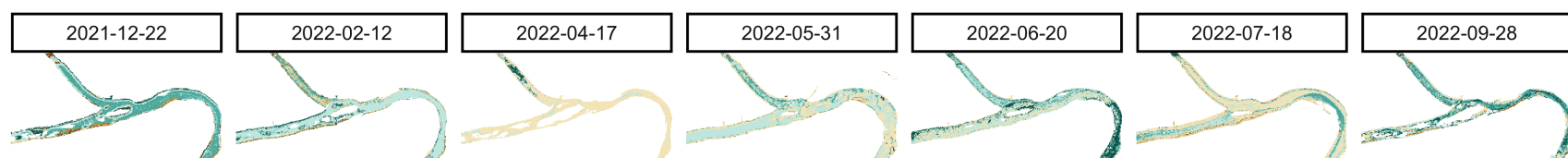
Table 5. Cross-date summary (mean \pm SD and range) of per-pixel performance across seven held-out dates.

Model	Metric	Mean	SD	Range
Semi-Supervised	Accuracy	0.149	0.060	0.052–0.218
	Kappa	-0.001	0.026	-0.040–0.036
Supervised	Accuracy	0.208	0.083	0.084–0.352
	Kappa	0.026	0.024	-0.006–0.058

(a) Observed (HEC-RAS-derived) Mesohabitats



(b) Modeled Mesohabitats (Supervised)



(c) Modeled Mesohabitats (Semi-supervised)

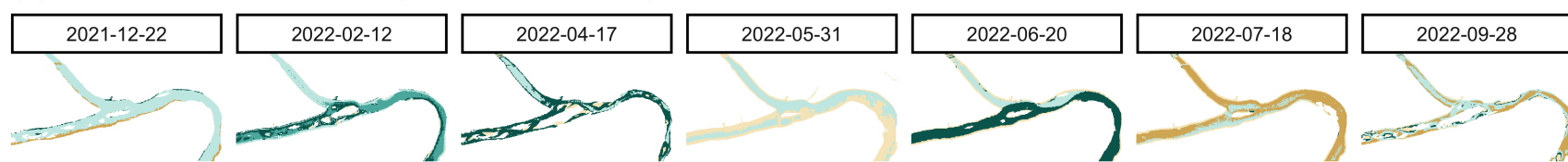


Fig. 10. Mesohabitat maps across seven dates at the Big Blue–Kansas River confluence. (a) Observed mesohabitat labels from the HEC-RAS–derived hydraulic model (Shallow Pool, Med Pool, Deep Pool, Fast Riffle, Raceway, Faster-than-a-Raceway, Faster-than-a-Deep-Pool).(b) Supervised (Random Forest; “Supervised”) image-based predictions from PlanetScope features (blue, green, red, NIR plus NDVI, NDWI, and NBR). (c) Semi-supervised (K-means plus majority label) image-based predictions from the same PlanetScope feature set. Facets are individual acquisition/model dates, ordered chronologically; all rasters are co-registered to the mesohabitat grid and aggregated to 15 m for display. Colors are consistent across rows and correspond to the eight classes noted in the legend.

4 Discussion

4.1 Summary of Principal Findings

Two complementary targets were evaluated. First, inundation (water vs. non-water) within the river corridor was recovered with high agreement using the semi-supervised pipeline (accuracy = 0.88; $k = 0.73$), exceeding the supervised baseline (Table 3; Fig. 6). This indicates strong and temporally stable spectral separability of open water at the working scale, consistent with the efficacy of visible–NIR contrasts and water indices for surface-water mapping (Jin et al., 2021). Second, direct prediction of mesohabitat labels (Shallow/Med/Deep Pool; Slow/Fast Riffle; Raceway; Faster-than-a-Raceway; Faster-than-a-Deep-Pool) using a leave-one-date-out design yielded modest cross-date performance (mean per-pixel accuracy $\approx 0.20\text{--}0.21$; mean $k \approx 0.02$), with substantial fold-to-fold variability linked to class composition and discharge state (Tables 4, 5). Despite low absolute metrics, prediction maps show coherent spatial structure (e.g., pool-like classes along the thalweg; high-velocity classes near constrictions; Fig. 10), indicating a learnable signal from four-band PlanetScope features even after aggregation.

4.1.1 Interpretation of Inundation Results

The semi-supervised pipeline yielded six clusters that were readily consolidated into five land-cover labels. Within the river corridor, impervious and bare substrates were not reliably separable spectrally; treating mixed/impervious pixels as “bare land” was appropriate given the absence of in-channel infrastructure aside from static bridge decks, which do not affect temporal comparisons. Choice of the cluster count (k) remains subjective and was fixed for consistency; a formal sensitivity analysis (varying k , band sets, and date combinations) was not undertaken here but would clarify stability versus over-partitioning trade-offs under noisy conditions (Vahidi et al., 2023).

Across sensors, the semi-supervised change signal was comparatively insensitive to input resolution. PlanetScope at ~ 3 m captured finer temporal variation in areal change, as expected, yet Landsat-9 at 30 m produced change patterns that were directionally consistent and of similar magnitude. This concordance indicates that rapid, lower-resolution deployments can recover robust mesoscale trends, while higher-resolution inputs refine the amplitude and spatial detail of detected changes.

4.1.2 Interpretation of Mesohabitat Results

Given mean per-pixel accuracies of 0.149 (semi-supervised) and 0.208 (supervised) with mean Cohen’s kappa of -0.001 and 0.026, respectively (Tables 4, 5), direct mesohabitat classification from four-band PlanetScope features at the aggregated support performs at or only slightly above chance, with the semi-supervised variant occasionally below chance. This outcome is consistent with several interacting factors. First, class boundaries are flow-dependent and nonstationary: mesohabitats translate, expand, and contract with discharge

and local hydraulics, so a given pixel can change label across dates, penalizing cross-date generalization unless hydrodynamic context is encoded Harris et al. (2024). Second, aggregation to ~15 m introduces sub-pixel mixing in narrow channels and along riffle pool transitions, attenuating spectral contrast and blurring boundaries. Third, several mesohabitat distinctions are spectrally ambiguous at four bands because they are partly morphodynamic states; much of their separability is carried by surface-texture and morphological cues (e.g., roughness patterns, local slope/curvature) not modeled here Moortgat et al. (2022). Class imbalance further limits parameter learning; some classes are sparse or absent in particular folds—even with inverse-frequency weighting Ma et al. (2019). Finally, label noise from model such that image mismatch (e.g. minor timing offsets between imagery and hydraulics, bathymetric uncertainty, co-registration drift) propagates into the categorical targets and caps attainable kappa under stringent cross-date validation. Under these constraints, near-zero, and occasionally negative kappa values are expected at the aggregated grain with a purely spectral feature set; nonetheless, qualitative spatial coherence in predicted maps suggests partial signal that could be amplified by adding texture and morphological context.

4.2 Sources of Error and Uncertainty

Three error modes were most evident: (i) edge confusion at unit boundaries where mixed pixels dominate; (ii) systematic bias toward dominant classes in the semi-supervised cluster-to-label step when clusters straddle multiple units; and (iii) fold-specific shocks when rare classes vanish from training or test, producing unstable per-fold k . These behaviors mirror sensitivities reported in object- and pixel-based riverscape mapping where segmentation parameters, illumination, and turbidity modulate separability (Demarchi et al., 2016a; Kutz et al., 2022; Zhang et al., 2023). Uncertainty quantification (e.g., entropy of class probabilities) was not computed here but is recommended to flag ambiguous zones for analyst review.

4.3 Practical implications

From a monitoring standpoint, the inundation pipeline is deployment-ready for tracking wetted area and corridor dynamics through time. The mesohabitat pipeline should be treated as proof-of-concept: it reveals where image-only predictors already align with hydraulic classes and where additional information is required to meet decision thresholds (e.g., habitat suitability modeling, restoration design). Importantly, the results support a tiered product strategy: use surface water maps operationally and generate mesohabitat layers where data richness permits.

4.4 Future considerations

Targeted enhancements are expected to materially improve mesohabitat accuracy and kappa:

- Restore native spatial support (~ 3 m) and add texture metrics (e.g., Gray-Level Co-occurrence Matrix [GLCM] contrast, entropy, local variance) to encode surface roughness and flow streaking (Farwell et al., 2021).
- Incorporate morphological context from DEM-derived slope/curvature or shallow bathymetry proxies where available, aligning with evidence that OBIA/terrain fusion improves riverscape unit mapping (Demarchi et al., 2016a).
- Adopt a hierarchical classifier (i.e. water to unit family to subclass) to reduce confusability among fine classes and stabilize minority categories.
- Explore spatial models (e.g., shallow CNN on PlanetScope tiles or RF with engineered texture windows) to inject neighborhood context beyond pixel spectra (Ma et al., 2019; Moortgat et al., 2022).
- Use cost-sensitive learning and focal sampling for rare classes; consider active learning to prioritize annotation where uncertainty is high (Maskey et al., 2018).
- Where feasible, evaluate hybrid/physics-informed fusion that brings co-registered hydraulic predictors (i.e. depth/velocity rasters) alongside imagery, an approach likely to raise ceiling performance (Harris et al., 2024).
- Quantify predictive uncertainty (e.g. calibration), enabling conservative products for management use.

4.5 Conclusion

Satellite-based workflows accurately recover inundation within river corridors and offer a scalable foundation for riverscape monitoring. Direct mesohabitat prediction from four-band PlanetScope features at aggregated resolution yields modest cross-date accuracy but exhibits meaningful spatial structure, indicating that mesohabitat signal is present and partially learnable. The path to decision-grade products is clear: use fine spatial resolution where possible, enrich features with texture and morphology, adopt hierarchical/imbalance-aware learning, and, where available, fuse hydraulics. Together, these steps align with the broader trajectory in high-resolution RS and ecohydraulics toward routine, basin-scale mapping of mesoscale habitat structure (Moortgat et al., 2022; Verma et al., 2021; Wegscheider et al., 2020).

Author Contributions

E.C.: conceptualization, methodology, software, formal analysis, investigation, data management, writing - original and draft, visualization, funding acquisition. **A.H.**: conceptualization, supervision, validation and QAQC, review and editing, resources, writing - review and editing, funding acquisition, and project administration.

Funding

The project was funded by the US Army Corps of Engineers' (USACE) Aquatic and Nuisance Species Research Program focus on Next Generation Ecological Modeling. This

research was supported in part by an appointment to the Department of Defense (DOD) Research Participation Program administered by the Oak Ridge Institute for Science and Education (ORISE) through an interagency agreement between the U.S. Department of Energy (DOE) and the DOD. ORISE is managed by ORAU under DOE contract number DE-SC0014664. All opinions expressed in this paper are the author's and do not necessarily reflect the policies and views of DOD, DOE, or ORAU/ORISE.

Acknowledgements

E.C. gratefully acknowledges the Environmental Laboratory of the USACE Engineer Research and Development Center (ERDC) and **A.H.** for funding, data access, and technical support that enabled this research. **E.C.** also acknowledges the Department of Marine Sciences at the University of Puerto Rico–Mayagüez for logistical and academic support during graduate research and dissertation-related activities.

Conflict of Interest

The authors declare no competing interests.

Availability of data and materials

The stream discharge data were retrieved from the USGS (De Cicco et al., 2023). The 30-m Landsat-9 satellite imagery can be retrieved from the USGS Landsat Collection (USGS, 2023c). The 3-m PlanetScope satellite imagery was accessed under a research license provided by Planet Labs (Planet Labs PBC, 2024), enabling the use of the data for academic purposes. The data that support the findings of this study are available from the corresponding author upon reasonable request. The river corridor shapefile and R code used for this analysis has been uploaded to Github and made publicly available via a General Public Use License. The repository can be accessed with the following link: <<https://github.com/el-cordero/meso-change.git>>

References

- Aadland, L., 1993. Stream Habitat Types: Their Fish Assemblages and Relationship to Flow. North American Journal of Fisheries Management 13, 790–806. [https://doi.org/10.1577/1548-8675\(1993\)013%3C0790:SHTTFA%3E2.3.CO;2](https://doi.org/10.1577/1548-8675(1993)013%3C0790:SHTTFA%3E2.3.CO;2)
- Aggarwal, C.C., 2018. Neural Networks and Deep Learning: A Textbook. Springer International Publishing, Cham. <https://doi.org/10.1007/978-3-319-94463-0>
- Anderson, J.R., Hardy, E.E., Roach, J.T., Witmer, R.E., 1976. A Land Use and Land Cover Classification System for Use with Remote Sensor Data (No. 964). United States Geological Survey.
- Aybar, C., Loaiza, D., Barja, A., Herrera, F., Gonzales, A., Espinoza, W., 2024. Combining R and earth engine, in: Cardille, J.A., Crowley, M.A., Saah, D., Clinton, N.E. (Eds.), Cloud-Based Remote Sensing with Google Earth Engine. pp. 629–651. https://doi.org/10.1007/978-3-031-26588-4_31
- Aybar, C., Wu, Q., Bautista, L., Yali, R., Barja, A., 2020. *Rgee*: An R package for interacting with Google Earth Engine. Journal of Open Source Software 5, 2272. <https://doi.org/10.21105/joss.02272>
- Brostow, G.J., Fauqueur, J., Cipolla, R., 2009. Semantic object classes in video: A high-definition ground truth database. Pattern Recognition Letters 30, 88–97. <https://doi.org/10.1016/j.patrec.2008.04.005>
- Calderon, M.S., An, K.-G., 2016. An influence of mesohabitat structures (pool, riffle, and run) and land-use pattern on the index of biological integrity in the Geum River watershed. Journal of Ecology and Environment 40, 13. <https://doi.org/10.1186/s41610-016-0018-8>
- Cavender-Bares, J., Schneider, F.D., Santos, M.J., Armstrong, A., Carnaval, A., Dahlin, K.M., Fatoyinbo, L., Hurt, G.C., Schimel, D., Townsend, P.A., Ustin, S.L., Wang, Z., Wilson, A.M., 2022. Integrating remote sensing with ecology and evolution to advance biodiversity conservation. Nature Ecology & Evolution 6, 506–519. <https://doi.org/10.1038/s41559-022-01702-5>
- Choukiker, S.K., Dohare, D., 2021. A Literature Review on Land Use Land Cover Changes Detection using Remote Sensing and GIS. International Journal for Research in Applied Science and Engineering Technology 9, 725–735. <https://doi.org/10.22214/ijraset.2021.33349>
- De Cicco, L.A., Hirsch, R.M., Lorenz, D., Watkins, D., Johnson, M., 2023. *dataRetrieval*: R packages for discovering and retrieving water data available from U.S. Federal hydrologic web services. <https://doi.org/10.5066/P9X4L3GE>
- Demarchi, L., Bizzi, S., Piégay, H., 2016a. Hierarchical Object-Based Mapping of Riverscape Units and in-Stream Mesohabitats Using LiDAR and VHR Imagery. Remote Sensing 8, 97. <https://doi.org/10.3390/rs8020097>
- Demarchi, L., Bizzi, S., Piégay, H., 2016b. Hierarchical Object-Based Mapping of Riverscape Units and in-Stream Mesohabitats Using LiDAR and VHR Imagery. Remote Sensing 8, 97. <https://doi.org/10.3390/rs8020097>
- Demir, I., Koperski, K., Lindenbaum, D., Pang, G., Huang, J., Basu, S., Hughes, F., Tuia, D., Raskar, R., 2018. DeepGlobe 2018: A Challenge to Parse the Earth through

- Satellite Images, in: 2018 IEEE/CVF Conference on Computer Vision and Pattern Recognition Workshops (CVPRW). IEEE, Salt Lake City, UT, USA, pp. 172–17209. <https://doi.org/10.1109/CVPRW.2018.00031>
- Eltayeb Elmalhal, A., Mahmoud Ibrahim Musa, M., 2023. Spatial Cloud Computing Using Google Earth Engine and R Packages, in: Geographic Information Systems - Data Science Approach [Working Title]. IntechOpen. <https://doi.org/10.5772/intechopen.1002686>
- Farwell, L.S., Gudex-Cross, D., Anise, I.E., Bosch, M.J., Olah, A.M., Radeloff, V.C., Razenkova, E., Rogova, N., Silveira, E.M.O., Smith, M.M., Pidgeon, A.M., 2021. Satellite image texture captures vegetation heterogeneity and explains patterns of bird richness. *Remote Sensing of Environment* 253, 112175. <https://doi.org/10.1016/j.rse.2020.112175>
- Fix, E., Hodges, J.L., 1989. Discriminatory Analysis. Nonparametric Discrimination: Consistency Properties. *International Statistical Review / Revue Internationale de Statistique* 57, 238. <https://doi.org/10.2307/1403797>
- Ganesh, B., Vincent, S., Pathan, S., Benitez, S.R.G., 2023. Integration of GIS and Machine Learning Techniques for Mapping the Landslide-Prone Areas in the State of Goa, India. *Journal of the Indian Society of Remote Sensing* 51, 1479–1491. <https://doi.org/10.1007/s12524-023-01707-y>
- Griffin, S., Lasko, J.C., 2020. Using Unmanned Aircraft System (UAS) and Satellite Imagery to Map Aquatic and Terrestrial Vegetation (No. ERDC/GRL TN-20-4). U.S. Army Engineer Research and Development Center, Vicksburg, MS. <https://doi.org/10.21236/ADA572123>
- Harris, A., Porter, M., McKay, S.K., Mulchandani, A., Stone, M., 2024. Hydraulic analysis for assessing environmental flow selection and ecological model formulation. *Ecohydrology* 17, e2681. <https://doi.org/10.1002/eco.2681>
- Hartigan, J.A., Wong, M.A., 1979. Algorithm AS 136: A K-Means Clustering Algorithm. *Applied Statistics* 28, 100. <https://doi.org/10.2307/2346830>
- Hernández, D., 2023. Using the tidyverse with terra objects: The tidyterra package. *Journal of Open Source Software* 8, 5751. <https://doi.org/10.21105/joss.05751>
- Hijmans, R.J., 2024. *Terra*: Spatial Data Analysis.
- Howard, J., Gugger, S., 2020. Deep learning for coders with fastai and PyTorch: AI applications without a PhD, First edition. ed. O'Reilly, Beijing Boston Farnham Sebastopol Tokyo.
- Jin, S., Liu, Y., Fagherazzi, S., Mi, H., Qiao, G., Xu, W., Sun, C., Liu, Y., Zhao, B., Fichot, C.G., 2021. River body extraction from sentinel-2A/B MSI images based on an adaptive multi-scale region growth method. *Remote Sensing of Environment* 255, 112297. <https://doi.org/10.1016/j.rse.2021.112297>
- Johansen, R.A., Reif, M.K., Saltus, C.L., Pokrzywinski, K.L., 2022. Using Unmanned Aircraft System (UAS) and Satellite Imagery to Map Aquatic and Terrestrial Vegetation (No. ERDC/EL SR-22-2). U.S. Army Engineer Research and Development Center Environmental Laboratory, Vicksburg, MS. <https://doi.org/10.21236/ADA572123>
- Kuhn, M., 2008. Building predictive models in R using the caret package. *Journal of Statistical Software* 28, 1–26. <https://doi.org/10.18637/jss.v028.i05>
- Kuhn, M., Wickham, H., 2020. Tidymodels: A collection of packages for modeling and machine learning using tidyverse principles.
- Kutz, K., Cook, Z., Linderman, M., 2022. Object based classification of a riparian environment

- using ultra-high resolution imagery, hierarchical landcover structures, and image texture. *Scientific Reports* 12, 11291. <https://doi.org/10.1038/s41598-022-14757-y>
- Lantz, B., 2023. Machine Learning with R, Fourth. ed. Packt Publishing Ltd, Birmingham, U.K.
- Li, Y., Zhang, H., Xue, X., Jiang, Y., Shen, Q., 2018. Deep learning for remote sensing image classification: A survey. *WIREs Data Mining and Knowledge Discovery* 8, e1264. <https://doi.org/10.1002/widm.1264>
- Lim, K., Jin, D., Kim, C.-S., 2018. Change Detection in High Resolution Satellite Images Using an Ensemble of Convolutional Neural Networks, in: 2018 Asia-Pacific Signal and Information Processing Association Annual Summit and Conference (APSIPA ASC). IEEE, Honolulu, HI, USA, pp. 509–515. <https://doi.org/10.23919/APSIPA.2018.8659603>
- Lindenschmidt, K.-E., Carr, M., 2018. Geospatial Modeling of River Systems. *Water* 10, 282. <https://doi.org/10.3390/w10030282>
- Ma, L., Liu, Y., Zhang, X., Ye, Y., Yin, G., Johnson, B.A., 2019. Deep learning in remote sensing applications: A meta-analysis and review. *ISPRS Journal of Photogrammetry and Remote Sensing* 152, 166–177. <https://doi.org/10.1016/j.isprsjprs.2019.04.015>
- Mandlik, G.G., Mundhe, R.N., 2018. A Review of Remote Sensing Techniques For Land Use Land Cover Change Detection Techniques. *Journal of Emerging Technologies and Innovative Research* 5, 900–902.
- Marcus, W.A., Fonstad, M.A., 2010. Remote sensing of rivers: The emergence of a sub-discipline in the river sciences. *Earth Surface Processes and Landforms* 35, 1867–1872. <https://doi.org/10.1002/esp.2094>
- Maskey, M., Ramachandran, R., Miller, J.J., Zhang, J., Gurung, I., 2018. Earth Science Deep Learning: Applications and Lessons Learned, in: IGARSS 2018 - 2018 IEEE International Geoscience and Remote Sensing Symposium. IEEE, Valencia, pp. 1760–1763. <https://doi.org/10.1109/IGARSS.2018.8517346>
- McKay, S.K., Mahan, V., Dougherty, M.P., Swannack, T.M., Hall, C., Saltus, C.L., Reif, M.K., Allen, S., 2022. New York Bight Ecological Model (NYBEM), Version 1.0.0. USACE, Environmental Laboratory.
- Moortgat, J., Li, Z., Durand, M., Howat, I., Yadav, B., Dai, C., 2022. Deep learning models for river classification at sub-meter resolutions from multispectral and panchromatic commercial satellite imagery. *Remote Sensing of Environment* 282, 113279. <https://doi.org/10.1016/j.rse.2022.113279>
- Niedballa, J., Axtner, J., Döbert, T.F., Tilker, A., Nguyen, A., Wong, S.T., Fiderer, C., Heurich, M., Wilting, A., 2022. Imageseg: An R package for deep learning-based image segmentation. *Methods in Ecology and Evolution* 13, 2363–2371. <https://doi.org/10.1111/2041-210X.13984>
- Planet Labs PBC, 2024. Planet application program interface: In space for life on earth.
- QGIS Development Team, 2024. QGIS Geographic Information System.
- R Core Team, 2023. *R*: A language and environment for statistical computing.
- Romero, A., Gatta, C., Camps-Valls, G., 2016. Unsupervised Deep Feature Extraction for Remote Sensing Image Classification. *IEEE Transactions on Geoscience and Remote Sensing* 54, 1349–1362. <https://doi.org/10.1109/TGRS.2015.2478379>
- Schwartz, J., 2016. Use of Ecohydraulic-Based Mesohabitat Classification and Fish Species Traits for Stream Restoration Design. *Water* 8, 520. <https://doi.org/10.3390/w8110520>

- Shabat, A.M., Tapamo, J.-R., 2017. A comparative study of the use of local directional pattern for texture-based informal settlement classification. *Journal of Applied Research and Technology* 15, 250–258. <https://doi.org/10.1016/j.jart.2016.12.009>
- Shashikant, 2019. Convolutional Neural Network: A Step By Step Guide. towards data science.
- Suir, G.M., Jackson, S., Saltus, C., Reif, M., 2023. Multi-Temporal Trend Analysis of Coastal Vegetation Using Metrics Derived from Hyperspectral and LiDAR Data. *Remote Sensing* 15, 2098. <https://doi.org/10.3390/rs15082098>
- Suttidate, N., Pidgeon, A.M., Hobi, M.L., Round, P.D., Dubinin, M., Radeloff, V.C., 2023. The effects of habitat heterogeneity, as measured by satellite image texture, on tropical forest bird distributions. *Biological Conservation* 281, 110002. <https://doi.org/10.1016/j.biocon.2023.110002>
- Thompson, D., Brodrick, P., 2021. Realizing Machine Learning's Promise in Geoscience Remote Sensing. *Eos* 102. <https://doi.org/10.1029/2021EO160605>
- USDA, n.d. National Agriculture Imagery Program (NAIP) GeoHub.
- USGS, 2023c. Landsat Collection.
- USGS, 2023a. USGS 1 Meter 14 X71y435 KS_Statewide_2018_A18.
- USGS, 2023b. USGS 1 Meter 14 X71y434 KS_Statewide_2018_A18.
- USGS, 2023d. USGS Watershed Boundary Dataset (WBD) for Kansas.
- USGS, 2011. High Resolution Orthoimagery Manhattan-Riley Co,KS.
- Vahidi, M., Aghakhani, S., Martín, D., Aminzadeh, H., Kaveh, M., 2023. Optimal band selection using evolutionary machine learning to improve the accuracy of hyper-spectral images classification: A novel migration-based particle swarm optimization. *Journal of Classification* 40. <https://doi.org/10.1007/s00357-023-09448-w>
- Van Rooijen, E., Lotsari, E., 2024. The spatiotemporal distribution of river bank erosion events and their drivers in seasonally frozen regions. *Geomorphology* 454, 109140. <https://doi.org/10.1016/j.geomorph.2024.109140>
- Verma, U., Chauhan, A., M. M., M.P., Pai, R., 2021. DeepRivWidth : Deep learning based semantic segmentation approach for river identification and width measurement in SAR images of Coastal Karnataka. *Computers & Geosciences* 154, 104805. <https://doi.org/10.1016/j.cageo.2021.104805>
- Wang, J., Kuffer, M., Roy, D., Pfeffer, K., 2019. Deprivation pockets through the lens of convolutional neural networks. *Remote Sensing of Environment* 234, 111448. <https://doi.org/10.1016/j.rse.2019.111448>
- Wegscheider, B., Linnansaari, T., Curry, R.A., 2020. Mesohabitat modelling in fish ecology: A global synthesis. *Fish and Fisheries* 21, 927–939. <https://doi.org/10.1111/faf.12477>
- Wiest, S., Harris, A., Hernandez-Abrams, D., 2024. Hydraulic model (HEC-RAS) of downstream of Tuttle Creek Reservoir at the confluence of the Big Blue River and the Kansas River near Manhattan, KS. <https://doi.org/10.5061/DRYAD.K3J9KD5GR>
- Wurm, M., Stark, T., Zhu, X.X., Weigand, M., Taubenböck, H., 2019. Semantic segmentation of slums in satellite images using transfer learning on fully convolutional neural networks. *ISPRS Journal of Photogrammetry and Remote Sensing* 150, 59–69. <https://doi.org/10.1016/j.isprsjprs.2019.02.006>
- Zaimis, G.N., Tamparopoulos, A.E., Tufekcioglu, M., Schultz, R.C., 2021. Understanding stream bank erosion and deposition in Iowa, USA: A seven year study along streams in

- different regions with different riparian land-uses. Journal of Environmental Management 287, 112352. <https://doi.org/10.1016/j.jenvman.2021.112352>
- Zhang, H., Jiang, Z., Zheng, G., Yao, X., 2023. Semantic Segmentation of High-Resolution Remote Sensing Images with Improved U-Net Based on Transfer Learning. International Journal of Computational Intelligence Systems 16, 181. <https://doi.org/10.1007/s44196-023-00364-w>
- Zimmermann, N., Washington-Allen, R., Ramsey, R., Schaeppman, M., Mathys, L., Koetz, B., Kneubuehler, M., Edwards, T., 2007. Modern Remote Sensing for Environmental Monitoring of Landscape States and Trajectories. pp. 65–91. https://doi.org/10.1007/978-1-4020-4436-6_6